

# 1 **TRMM MICROWAVE IMAGER (TMI) ALIGNMENT AND ALONG-SCAN BIAS**

## 2 **CORRECTIONS**

3 *Rachael Kroodsma<sup>1</sup>, Stephen Bilanow<sup>2</sup>, and Darren McKague<sup>3</sup>*

4 <sup>1</sup>ESSIC, University of Maryland / NASA Goddard Space Flight Center

5 <sup>2</sup>SGT Inc. / NASA Goddard Space Flight Center

6 <sup>3</sup>University of Michigan

7 Corresponding author email: rachael.a.kroodsma@nasa.gov

### 9 **ABSTRACT**

10 The Tropical Rainfall Measuring Mission (TRMM) Microwave Imager (TMI) dataset released  
11 by the Precipitation Processing System (PPS) has been updated to a final version following the  
12 decommissioning of the TRMM satellite in April 2015. The updates are based on increased  
13 knowledge of radiometer calibration and sensor performance issues. In particular, the Global  
14 Precipitation Measurement (GPM) Microwave Imager (GMI) is used as a model for many of the  
15 TMI updates. This paper discusses two aspects of the TMI data product that have been  
16 reanalyzed and updated: alignment and along-scan bias corrections. The TMI pointing accuracy  
17 is significantly improved over prior PPS versions, which used at-launch alignment values. A  
18 TMI instrument mounting offset is discovered as well as new alignment offsets for the two TMI  
19 feedhorns. The original TMI along-scan antenna temperature bias correction is found to be  
20 generally accurate over-ocean, but a scene temperature-dependent correction is needed to  
21 account for edge-of-scan obstruction. These updates are incorporated into the final TMI data  
22 version, improving the quality of the data product and ensuring accurate geophysical parameters  
23 can be derived from TMI.

## 1 *1. INTRODUCTION*

2 The Tropical Rainfall Measuring Mission (TRMM) was launched in November 1997 carrying  
3 onboard the TRMM Microwave Imager (TMI) and Precipitation Radar (PR) as the primary  
4 instruments to measure rainfall (Kummerow et al. 1998). After a successful 17+ years of  
5 operation, the spacecraft was decommissioned in April 2015 as the orbit decayed and the  
6 spacecraft altitude dropped below 350 km, a result of the fuel onboard running out in July 2014.  
7 As part of end-of-mission activities, the TRMM data products have been reanalyzed and updated  
8 to a final version 8 (V8), replacing the previous version 7 (V7) data products that were released  
9 in 2011 (Stocker et al. 2018). This paper describes two major updates to the TMI V8 data  
10 product.

11 Shortly after TRMM was launched, an extensive post-launch analysis of the TMI data  
12 was performed by Wentz et al. (2001) to correct TMI calibration issues. While microwave  
13 radiometers are tested prior to launch, there are many factors that impact the instrument on-orbit  
14 in the space environment that cannot be accounted for pre-launch, such as solar intrusions  
15 (Kunkee et al. 2008), field-of-view obstructions (McKague et al. 2011), thermal variations  
16 (Gopalan et al. 2009), and alignment errors (Poe et al. 2008). These issues are identified and  
17 corrected post-launch using the on-orbit data. Since the launch of TRMM, several other  
18 radiometers have been launched, leading to a greater understanding of potential radiometer  
19 calibration issues and how to correct for them. As a result, radiometer designs have improved  
20 and the algorithms to analyze on-orbit data have advanced, as evidenced most recently by the  
21 Global Precipitation Measurement (GPM) Microwave Imager (GMI), acknowledged as a very  
22 stable and accurate microwave radiometer due to design enhancements and on-orbit data analysis  
23 (Draper et al. 2015; Wentz and Draper 2016). The corrections included in TMI V8 are derived

1 based on this increased knowledge of other radiometer calibration issues, and in particular the  
2 GMI on-orbit analysis is used as a model for many of the TMI V8 updates.

3       There are several modifications that are incorporated in TMI V8 to improve the  
4 calibration and quality of the data product. This paper discusses two of these modifications: the  
5 alignment of the instrument and feedhorns and the along-scan temperature bias correction. Other  
6 corrections to TMI V8 include a hot load correction (Alquaied et al. 2018a), updated emissive  
7 antenna correction (Alquaied et al. 2018b), radio frequency interference flag (Draper 2018),  
8 improved calibration (Stocker et al. 2018), and intercalibration to GMI (Berg 2017). These  
9 corrections are included in the dataset released by the Precipitation Processing System (PPS).  
10 Wentz (2015) also provides a thorough analysis of the TMI mission data and derives similar  
11 corrections to the TMI data as are incorporated in the PPS TMI V8 dataset. However, Wentz  
12 describes corrections to TMI based on the Remote Sensing Systems (RSS) algorithms that are  
13 included in the data version released by RSS, whereas the corrections described here are based  
14 on PPS algorithms. In this paper, we also add an instrument alignment offset to update  
15 geolocation and analysis over warm targets to update an antenna temperature dependence of the  
16 along-scan bias correction beyond those performed by RSS.

17       In addition to updating the TMI data product, all spaceborne microwave radiometers with  
18 similar channels dating back to December 1997 will be incorporated into the GPM mission's  
19 constellation of radiometers. This constellation originally included only those radiometers in  
20 operation after the launch of GPM in February 2014 (Hou et al. 2014). Since TMI observations  
21 overlap with GMI, TMI can be used to intercalibrate radiometers that existed prior to the launch  
22 of GPM, resulting in a consistent dataset of historical observations. The GPM Intercalibration  
23 Working Group (XCAL) is responsible for calculating the intercalibration constants used for the

dataset (Berg et al. 2016). Since TMI makes up a significant portion of this intercalibration dataset and is used as a transfer for radiometers prior to GMI, the TMI V8 improvements are critical to ensure an accurate long-term data record that can be reliably used for climate studies.

## ***2. INSTRUMENT DESCRIPTION***

TMI was a 9-channel conical scanning microwave radiometer with an offset parabolic reflector viewing about  $49^\circ$  from nadir and an approximate Earth-view azimuthal rotation scan of  $130^\circ$  (Kummerow et al. 1998). The design was modeled after the Special Sensor Microwave Imager (SSM/I, Hollinger et al. 1990) and included similar channels to SSM/I centered at 19.35, 21.3, 37.0, and 85.5 GHz (referred to as 19, 21, 37, and 85 GHz). In addition, TMI included a lower frequency channel centered at 10.65 GHz to measure heavier rainfall (referred to as 10 GHz). The 19-85 GHz channels shared a feedhorn, while the 10 GHz channels were contained in a separate feedhorn. All channels measured both vertical and horizontal polarization (v/h-pol), except 21.3 GHz, which was only v-pol. The TMI instrument field-of-view swept a conical path about the instrument spin axis and sampled 104 pixels across the scan for the 10-37 GHz channels and 208 pixels for the higher resolution 85 GHz channels. A nominal azimuth start angle of  $-64.4024^\circ$  for the Earth-view scan was estimated prior to launch. The TMI spin rate of 31.6 rpm was observed to be extremely uniform, and the instrument clock controlled the sampling at even intervals of 3.3 milliseconds giving a rotation angle of  $0.6256^\circ$  between the high frequency samples.

## ***3. DESCRIPTION OF CORRECTIONS***

### ***a. Alignment***

The alignment parameters that we estimate in this paper encompass offsets in the instrument axes relative to the spacecraft axes and offsets in the scan cone half angle that result from feedhorn offsets. There are four alignment parameters that we adjust: (1) pitch: alignment bias about the instrument pitch axis, (2) roll: alignment bias about the instrument roll axis, (3) azimuth: adjustment of the start of sampling azimuth angle, or instrument yaw, and (4) cone: adjustment of scan cone half angle, or angular radius of scan cone. Items (3) and (4) have the possibility of different values for different channels due to feedhorn offsets. Previous TMI versions used values estimated prior to launch. We also include a time delay between the sampling of the multi-channel feedhorn and 10 GHz feedhorn that was not included in previous data versions. This delay is estimated to be 0.2238 seconds based on the angle of rotation between the two feedhorn positions.

#### *b. Along-Scan Temperature Bias*

The first post-launch analysis of TMI data noticed significant along-scan biases for many of the channels (Wentz et al. 2001). A simple offset versus scan position correction by channel was implemented to remove the biases in the data product. Over-ocean antenna temperatures (TAs) were averaged using various filters to derive a scan bias as a difference from the mean. This correction assumes that the scan biases are constant at all scene temperatures; however, recent analysis shows that this assumption is not correct. Similar along-scan biases were noticed in the GMI data shortly after it launched (Draper et al. 2015). There are two components to the GMI along-scan correction: (1) a magnetic interference correction and (2) a residual bias from antenna intrusions that includes a temperature-dependent correction for removing edge-of-scan obstructions. Item (1) was determined using ground measurements and item (2) was calculated

1 using on-orbit data. Some features in the TMI scan angle dependence may have an explanation  
2 similar to that suggested for GMI, but we do not have ground measurements from TMI to  
3 separate the two corrections. Therefore, a temperature-dependent along-scan correction is  
4 derived for TMI using on-orbit data that encompasses both potential magnetic interference and  
5 antenna intrusions.

#### 6 7 **4. PROCEDURE**

8 A complication with updating the TMI dataset is that some corrections are dependent on each  
9 other. Corrections were derived in sequence; i.e. we first updated two aspects of alignment (cone  
10 and azimuth) that impact geolocation and earth incidence angle (EIA). These values are needed  
11 to process our radiative transfer model for the along-scan correction. However, after analyzing  
12 the along-scan correction, we determined that we needed to further update other aspects of the  
13 alignment (pitch and roll), which in turn meant re-calculating the along-scan correction.  
14 Concurrently, several other groups within XCAL and PPS were evaluating various other updates  
15 to TMI V8. PPS reprocessed the TMI dataset several times during this revision period to ensure  
16 that all the corrections are accurate and complement each other. This section will discuss the  
17 procedure for deriving the alignment and along-scan bias corrections, and the following section  
18 will present the results of the analysis.

##### 19 20 *a. Alignment Corrections for Cone and Azimuth Angles using Geolocation*

21 Alignment errors show up in their effects on image pixel geolocation. The alignment of TMI is  
22 examined by creating maps of gridded antenna temperatures (TAs) for the two spacecraft yaw  
23 orientations. In order to keep the sun on one side of the spacecraft for thermal control, the

1 TRMM spacecraft yawed 180 degrees every two to four weeks, thereby switching TMI from a  
2 forward to backward looking orientation. The effect of an alignment error on pixel coordinates  
3 will generally be different for the forward look of the instrument than for the backward look.  
4 There is a large contrast between land and ocean TAs at microwave imager frequencies, so small  
5 offsets in geolocation cause coastlines to appear highlighted when taking the difference between  
6 the forward and backward looking maps of observed TAs. This method has been used with great  
7 success for various sun-synchronous orbiters by taking the difference between ascending and  
8 descending passes (e.g. Berg et al. 2013; Moradi et al. 2013). With the  $98^\circ$  inclination of sun-  
9 synchronous orbits, the flight directions of the ascending and descending orbits when crossing  
10 the equator are nearly opposite. This means various alignment biases have nearly opposite effects  
11 on the pixel geolocation. However, for TRMM's non-sun-synchronous  $35^\circ$  inclination orbit, the  
12 difference in flight direction when crossing the equator is approximately  $70^\circ$ . Therefore,  
13 TRMM's two yaw orientations are used for alignment analysis since they have nearly opposite  
14 effects from the yaw 0 versus the yaw 180 flight (fore- versus aft-viewing) cases.

15 Figure 1 shows  $0.1^\circ$  gridded Yaw 0 – Yaw 180 TAs for observations from 2004 using V7  
16 geolocation over South America. The TMI geolocation algorithm is a line of sight intersection  
17 with a WGS-84 Earth ellipsoid model. Topography is not considered due to the large footprint  
18 sizes. This does not impact our geolocation analysis as we are only concerned with coastlines.  
19 The South America region is chosen for analysis due to its proximity around the equator and the  
20 variety of coastline directions. Proximity to the equator reduces error due to incomplete sampling  
21 across the scan at the higher latitudes of the TRMM orbit, and the variety of coastlines ensures  
22 that this method is valid for all directions. The coastlines in Fig. 1 are apparent in several  
23 channels, most notably in 10h. This indicates that the V7 alignment is incorrect and needs to be

1 updated. The TRMM spacecraft attitude is tracked to about  $0.01^\circ$  as described in Stocker et al.  
2 (2018), therefore, this alignment error is attributed to the TMI instrument.

3 We chose to adjust the cone and azimuth angles as the first steps. In a rough sense the  
4 cone bias adjusts the coastline forward and back relative to the ground track, while the azimuth  
5 bias adjusts it left and right, so these two effects are fairly independent. To quantitatively assess  
6 the optimal cone and azimuth angles, a coast mask is applied to the Yaw 0 – Yaw 180 maps and  
7 the root mean square (RMS) of the TA difference is calculated, as shown in Fig. 2 for the 10  
8 GHz channels. The optimal alignment parameters will make the coastlines disappear as the RMS  
9 differences are minimized.

10 There are four primary steps to derive the alignment parameters: (1) vary the cone or  
11 azimuth angles and calculate the latitude and longitude for each TMI pixel, (2) grid the TAs by  
12 yaw orientation and calculate the Yaw 0 – Yaw 180 TA difference for each cone and azimuth  
13 value, (3) use the coastline mask to calculate the RMS for each angle, and (4) fit a 3<sup>rd</sup> order  
14 polynomial to the RMS as a function of cone/azimuth angle to find the angle associated with the  
15 minimum RMS. For Step 1, the cone angle is varied from  $49.0^\circ$  to  $49.6^\circ$  while holding the  
16 azimuth angle constant at  $-64.4^\circ$ , and the azimuth angle is varied from  $-64.5^\circ$  to  $-63.7^\circ$  holding  
17 the cone angle constant at  $49.0^\circ$ . This analysis assumes that the cone and azimuth angles are  
18 independent of each other, which was found to be a reasonable assumption. For Step 2, a  $0.1^\circ$   
19 grid size is used. This grid size was determined to be sufficient, since smaller grid sizes did not  
20 significantly impact our results and required more data to decrease noise and resulted in  
21 increased processing time. Three months of data from January to March 2004 are chosen as the  
22 test dataset. We found that this gives adequate sampling while keeping a reasonable processing  
23 time. Figure 3 shows the results of Step 4 for the 19v channel, where the RMS for each angle



(cone or azimuth) is plotted and a 3<sup>rd</sup> order polynomial is fit to the data. The angle where the RMS is at a minimum is chosen as the optimal cone/azimuth angle for that channel.

#### *b. Along-Scan Antenna Temperature Bias Correction*

At a given scan position, the observed TA can be decomposed into the desired on-Earth interference-free main-beam brightness temperature (TB)  $T_{b,mb}$ , and the contribution from interference/obstruction given the effective brightness of the source of interference  $T_{b,i}$  and the effective beam fraction of the interference  $f_i$  as (McKague et al. 2011):

$$TA = T_{b,mb} * (1 - f_i) + T_{b,i} * f_i \quad (1)$$

Estimating  $T_{b,i}$  and  $f_i$  at each scan position requires known measurements  $T_{b,mb}$ . This is done by using over-ocean observations from the vicarious cold calibration technique (Kroodasma et al. 2017) and over-land observations from the vicarious warm calibration technique (Yang et al. 2016). These biases can be linearly interpolated to compute the bias at an arbitrary scene temperature (McKague et al. 2011; Draper 2016). Since beam patterns as well as sources of interference vary from channel to channel, this is done independently for each channel. Figure 4 shows the TA along-scan biases calculated using the vicarious cold (blue line) and warm (red line) techniques. Both the cold and warm along-scan biases show similar patterns for the large- and small-scale fluctuations, such as the large bump in 21v and small ripples in 85h. These fluctuations are most likely due to internal magnetic interference as they are similar to those seen in GMI. The GMI 10h channel also displayed large bumps in the scan biases like TMI 21v due to that receiver being the closest to magnets on the instrument (Draper et al. 2015). Unfortunately, we do not have enough information about the TMI instrument to reach the same conclusion for why TMI 21v has the largest scan biases, but we hypothesize a similar reason. As with GMI, the

1 TMI scan fluctuations due to possible magnetic interference are constant with respect to scene  
2 temperature. However, there are two distinct differences in the cold and warm TMI biases. One  
3 is the edge-of-scan pattern attributed to an obstruction. The second is an overall curvature or  
4 slope pattern that is different for cold vs. warm along-scan biases, most notably in the v-pol  
5 channels.

### 6 7 *c. Alignment Effects on Along-Scan Antenna Temperature Biases*

8 Figure 4 shows that one main difference between the cold and warm along-scan biases is an  
9 overall curvature and and/or slope pattern. We ideally want to understand where this difference  
10 comes from and to correct the underlying problem if possible. One phenomenon that can cause  
11 some curvature and/or slope changes across the scan is a pitch and/or roll offset of the spacecraft  
12 (Kroodsma et al. 2012). Pitch and roll offsets directly affect the EIA of the radiometer, and the  
13 over-ocean cold biases are sensitive to EIA variations across the scan, whereas the warm biases  
14 are not. Roll changes give a roughly linear slope in EIA with scan angle, while pitch changes  
15 give a quadratic-like curvature versus scan angle. By contrast, a cone bias gives a constant EIA  
16 offset, while an azimuth bias does not affect the EIA.

17 Assuming that the large- and small-scale fluctuations in the along-scan biases are  
18 constant as a function of scene temperature, taking the difference between the cold and warm  
19 scan biases for the middle portion of the scan (to remove edge-of-scan effects) allows a pitch and  
20 roll offset to be calculated from the resulting pattern across the scan. Figure 5 shows the warm  
21 minus cold TA bias difference for the whole scan (black line) as well as a middle portion of the  
22 scan (green line). The exact sensitivity of TAs to EIA over cold ocean varies with channel, but  
23 roughly the TMI v-pol channels change by 2 K and h-pol channels by -1 K for every 1° EIA.

1 This behavior is reflected in Fig. 5 where the v-pol channels (left column) all show a similar  
2 variation across the scan, whereas the h-pol channels (right column) all exhibit similar but  
3 slightly opposite behavior from v-pol. Therefore, we conclude that this difference between cold  
4 and warm along-scan biases is due to EIA offsets from a pitch and/or roll offset. A rough  
5 evaluation of the mean slopes and curvatures for the middle of the scan in Fig. 5 indicates that a  
6 pitch and roll bias on the order of a tenth of degree is needed. To obtain a better estimation of the  
7 exact offsets, the method described in the next section was developed.

#### 8 9 *d. Alignment Corrections for Pitch and Roll Offsets using Geolocation*

10 Another method to examine a potential pitch/roll offset is to use the four-step geolocation  
11 analysis for calculating the cone angle as outlined in Section 3.a but to apply the analysis to  
12 different sections of the scan instead of using all scan positions together. A cone angle offset  
13 causes a constant geolocation shift across the scan, so the derived cone angle is the same at all  
14 scan positions. However, a pitch/roll offset results in a different pattern across the scan, as seen  
15 in Fig. 6, which models the geolocation of a TMI scan for nominal pointing (no pitch/roll offset,  
16  $49^\circ$  cone angle), a cone angle offset of  $+5^\circ$ , a pitch offset of  $+5^\circ$ , and a roll offset of  $+5^\circ$  (these  
17 values are exaggerated to see effect). This behavior can be used to distinguish between a  
18 pitch/roll offset and the cone angle by applying the geolocation analysis at different scan  
19 positions. With the axis of the scan nominally at nadir, the shifts in geolocation from pitch or roll  
20 biases give a different cone angle bias at different scan positions. Yaw alignment errors are not  
21 considered here since they have exactly the same effect as changes in the azimuth angle.  
22 Therefore, any yaw errors are incorporated in the updated azimuth start angle.

The geolocation analysis is applied to three subsets of scan positions at the left (10-30 scan positions low resolution, 20-60 scan positions high resolution), middle (40-60, 80-120), and right (70-90, 140-180) parts of the TMI scan. Using a range of scan positions for each subset allows sufficient sampling, and the far left and right edges of the scan are excluded to remove potential edge-of-scan obstructions. Results are discussed in the next section.

## 5. RESULTS

As noted in the previous section, our process for updating alignment and along-scan bias corrections is iterative. Initial values for cone and azimuth angles derived from geolocation difference mapping were used prior to closer inspection of along-scan antenna temperature biases. Patterns seen in these biases led to the new approach of geolocation difference mapping partitioned into three parts of the swath. In this section we use the methods described in the previous section to derive the instrument pitch and roll offsets, re-calculate the cone and azimuth angles using the pitch and roll offsets, and present the new along-scan bias correction based on the updated alignment.

### a. Instrument Pitch and Roll Offsets

Figure 7 shows the cone angle calculated for each subset of the scan for all channels. Two important observations can be made from this figure: (1) the 10 GHz channels differ significantly from the 19-85 GHz channels, which is attributed to the two feedhorns, and (2) there is a difference in the cone angle value across the scan that is relatively consistent for each feedhorn. For the pitch and roll calculation, we are concerned with observation (2). Note that the left, middle, and right subsets show very similar separations in their feedhorn groups even while the

mean values vary per channel. The left-right spread indicates the need for a roll correction, and the off-center middle result indicates the need for a pitch correction.

The derived cone angle across the scan is a function of azimuth, pitch, and roll angles. The pitch and roll offsets that result in the best-fit line to the cone angles of the three scan subsets are taken as the pitch and roll estimates for that channel. This best-fit line is iteratively derived using a Newton-Raphson technique and only takes two iterations to converge. The root mean square of the cone angles with the cone angle fits is less than  $0.005^\circ$  for all channels. Figure 8 shows this best-fit line for the 19v channel, and Fig. 9 gives the pitch and roll derived for all channels using this method. We do not expect the pitch or roll bias from instrument mounting offsets to be different for each channel, therefore, we choose the mean value of  $-0.08^\circ$  for both pitch and roll. There is some uncertainty associated with this calculation due to the limited data used and the geolocation method. We used the three-month test dataset described in Section 3.a for analysis. We also looked at other time periods early and late in the TRMM mission for validation and confirmed our results are consistent. The values calculated in Fig. 9 are from the South America region (Fig. 1) as well as a region that includes Indonesia to utilize more data. If just one of these regions is chosen rather than both, the pitch and roll offsets derived are slightly different. In addition to this uncertainty, Fig. 9 shows a spread for pitch and roll by channel. The spread in roll by channel is smaller than pitch, giving more confidence in its accuracy. It is not surprising that the pitch is less certain, given how it is picked out from the small curvature of the scan angle dependence. Based on the standard deviation from different regions and channels, we estimate the uncertainty in the pitch and roll estimates to be approximately  $0.03^\circ$  and  $0.01^\circ$ , respectively.

#### *b. Cone and Azimuth Angles*

1 The new pitch and roll offsets are input to the TMI dataset to re-calculate latitude and longitude.  
2 The fore/aft geolocation difference analysis is then applied using the pitch/roll offset of  $-0.08^\circ$  to  
3 re-derive the cone and azimuth angles. The results are shown in Fig. 10 for all channels. As  
4 noted previously, there is a significant difference between the 10 GHz channels and 19-85 GHz  
5 channels due to the different feedhorns. There is also a noticeable difference between the 10v  
6 and 10h cone angles. We believe that this difference is real, probably due to polarization phase  
7 center offsets in the feedhorn. Due to feedhorn design constraints, small phase center offsets may  
8 exist among channels contained in the same feedhorn (Ruf 2018). One solution to align the  
9 beams in a multi-frequency feedhorn is described in Imbriale (2006). We do not have  
10 information on what tests were performed on TMI to determine alignment of the phase centers,  
11 but there was some indication in ground measurements of a difference in the 10 GHz v- and h-  
12 pol cone angles (Shiue 1997). We decided to include this cone angle difference for the  
13 calculation of EIA since EIA accuracy is important in modeling the brightness temperatures.  
14 This results in separate EIAs reported for the 10v and 10h channels. However, only one  
15 geolocation is reported for both 10 GHz channels by using the average of the calculated 10v and  
16 10h cone angles. This simplifies the data structure and only causes an approximate geolocation  
17 error on the order of 1 km, which was deemed acceptable since the low frequency pixel sizes are  
18 over 40 km. The EIAs for 10v and 10h are calculated using a cone angle offset from the  
19 averaged cone angle. This offset is negative for 10v and positive for 10h. For all other channels a  
20 single EIA is reported since the difference in our estimates per channel are not considered  
21 significant.

22 Table 1 shows the average cone and azimuth start angles for the two feedhorns and the  
23 cone angle offset used to calculate EIA for the 10 GHz channels. The constants derived by

Wentz (2015) are also reported, and we show very similar results. The differences can be attributed to variations in our methods and different spacecraft and instrument attitude calculations. As with the pitch/roll geolocation analysis, we used the three-month test dataset to derive the cone and azimuth angles and then confirmed that the cone and azimuth angles remained constant throughout the TRMM mission. Figure 11 shows the updated TMI yaw difference maps using the new instrument pitch and roll offsets and the cone and azimuth angles from Table 1 for 2004. The alignment of all channels is greatly improved using the new constants compared to Fig. 1. Residual effects over the Andes still exist, which may be due to fore/aft sampling variations of the surface snow cover and the lack of topography in the geolocation algorithm. For example, Lake Titicaca at an altitude of 3.8 km shows clear coastline errors.

### *c. Along-Scan Bias Correction*

Once the pitch/roll offset is derived and the cone angle and azimuth angles are updated, the along-scan bias correction analysis can be re-applied. Figure 12 shows the new along-scan bias at both cold and warm TAs compared with V7. The V7 biases are the same for both cold and warm TAs since it is a constant additive bias regardless of scene temperature. The V8 along-scan biases are derived using the vicarious cold and warm techniques, accounting for the pitch/roll offset and calculating a bias at a given scene temperature according to Eq. 1. As seen in Fig. 12, the V8 cold and warm biases have greater agreement for the middle part of the scan compared to Fig. 4, giving us confidence that the correct pitch/roll offset has been applied. Figure 12 also shows the impact of using both cold and warm biases for correcting edge-of-scan obstructions. Version 7 assumed these biases were constant as a function of scene temperature, so it did not

capture the temperature-dependent scan biases near the edge of the scan. Version 8 differs from V7 at the edge of the scan for most channels but particularly for 19h and 37h, which differ by about 1 K at the right side of the scan.

## 6. SUMMARY

The TRMM data products from PPS have been updated to a final Version 8 following the decommissioning of the TRMM spacecraft in April 2015 after a very successful 17+ years of operation. This final version includes several corrections to TMI to improve the calibration and dataset quality. This paper described two improvements to the TMI dataset for V8: sensor alignment and along-scan bias corrections.

The sensor alignment was analyzed by creating geolocation maps of the antenna temperature difference between TMI forward and backward looks at coastlines. Prior versions used at-launch values for alignment that were found to not be correct. Using the geolocation maps, we updated the alignment to include an instrument pitch and roll offset of  $-0.08^\circ$  and  $-0.08^\circ$ , respectively, and we modified the cone and azimuth start angles to account for differences in the two feedhorns.

The along-scan bias correction was updated to include the effects of temperature-dependent edge-of-scan obstruction and the new instrument pitch and roll offset. Previous TMI versions used over-ocean TA biases to correct for along-scan biases, but we found this to be inadequate at all scene temperatures. Therefore, we used a linear interpolation between cold and warm TA references to derive a new correction for V8. The updated along-scan bias correction is very similar to the V7 correction with the large- and small-scale fluctuations, but there are two



1 main differences: the slight slope adjustment due to the inclusion of a pitch and roll offset, and  
2 the edge of scan differences due to the inclusion of the warm TA reference.

3 The two updates described here, along with the other updates for TMI V8, significantly  
4 improve the PPS-released TMI dataset. The alignment improvements do not directly affect the  
5 brightness temperatures; however, they do impact geolocation and the earth incidence angles,  
6 which are necessary to accurately model the TBs in retrieval algorithms. The along-scan bias  
7 correction directly impacts the TBs, and the effect on retrieval algorithms will be most  
8 pronounced near the edge of the scan, where the updated correction adjusts the TBs at warm  
9 scene temperatures by nearly 1 K for some channels. The alignment and along-scan bias  
10 improvements ensure an accurate TMI observational dataset that can be reliably used in retrieval  
11 algorithms and for studying long-term geophysical trends.

## 13 ***ACKNOWLEDGMENTS***

14 Funding for this work was provided by NASA's GPM mission and the NASA Precipitation  
15 Measurement Missions (PMM) science team under Grant NNX16AE38G.

## 17 ***REFERENCES***

18 Alquaied, F., R. Chen, and W. L. Jones, 2018a: Hot load temperature correction for TRMM  
19 Microwave Imager in the legacy brightness temperature, *IEEE J. Sel. Topics Appl. Earth Obser.*,  
20 *in review*.

Alquaied, F., R. Chen, and W. L. Jones, 2018b: Emissive reflector correction in the legacy version 1B11 V8 (GPM05) brightness temperature of the TRMM Microwave Imager, *IEEE J. Sel. Topics Appl. Earth Obser.*, doi:10.1109/JSTARS.2018.2797021, *in press*.

Berg, W., M. R. P. Sapiiano, J. Horsman and C. Kummerow, 2013: Improved geolocation and earth incidence angle information for a fundamental climate data record of the SSM/I sensors, *IEEE Trans. Geosci. Remote Sens.*, **51**, 1504-1513, doi:10.1109/TGRS.2012.2199761.

Berg, W., and Coauthors, 2016: Intercalibration of the GPM microwave radiometer constellation, *J. Atmos. Oceanic Technol.*, **33**, 2639-2654, doi:10.1175/JTECH-D-16-0100.1.

Berg, W., 2017: Towards developing a long-term high-quality intercalibrated TRMM/GPM radiometer dataset, *2017 IEEE International Geoscience and Remote Sensing Symposium: Proceedings*, pp. 248-250, doi:10.1109/IGARSS.2017.8126941.

Draper, D. W., D. A. Newell, F. J. Wentz, S. Krimchansky, and G. M. Skofronick-Jackson, 2015: The Global Precipitation Measurement (GPM) Microwave Imager (GMI): Instrument overview and early on-orbit performance, *IEEE J. Sel. Topics Appl. Earth Obser.*, **8**, 3452-3462, doi:10.1109/JSTARS.2015.2403303.

Draper, D., 2016: Calibration data book for Global Precipitation Measurement (GPM) Microwave Imager (GMI) Revision H, Ball Aerospace & Technologies Corp. Doc. No. 2344649.

1 Draper, D. W., 2018: Radio frequency environment for earth-observing passive microwave  
2 imagers, *IEEE J. Sel. Topics Appl. Earth Obser.*, doi:10.1109/JSTARS.2018.2801019, *in press*.  
3

4 Gopalan, K., W. L. Jones, S. Biswas, S. Bilanow, T. Wilheit, and T. Kasparis, 2009: A time-  
5 varying radiometric bias correction for the TRMM microwave imager, *IEEE Trans. Geosci.*  
6 *Remote Sens.*, **47**, 3722-3730, doi:10.1109/TGRS.2009.2028882.  
7

8 Hollinger, J. P., J. L. Peirce, and G. A. Poe, 1990: SSM/I instrument evaluation, *IEEE Trans.*  
9 *Geosci. Remote Sens.*, **28**, 781-790, doi:10.1109/36.58964.  
10

11 Hou, A. Y., and Coauthors, 2014: The Global Precipitation Measurement Mission, *Bull. Amer.*  
12 *Meteor. Soc.*, **95**, 701-722, doi:10.1175/BAMS-D-13-00164.1.  
13

14 Imbriale, W. A., 2006: *Spaceborne Antennas for Planetary Exploration*, John Wiley & Sons,  
15 Hoboken, NJ, 546 pp.  
16

17 Kroodsma, R., D. McKague, and C. Ruf, 2012: Satellite attitude analysis using the vicarious cold  
18 calibration method for microwave radiometers, 2012 *IEEE International Geoscience and Remote*  
19 *Sensing Symposium: Proceedings*, IEEE, 2964-2967, doi:10.1109/IGARSS.2012.6350804.  
20

21 Kroodsma, R. A., D. S. McKague, and C. S. Ruf, 2017: Vicarious cold calibration for conical  
22 scanning microwave imagers, *IEEE Trans. Geosci. Remote Sens.*, **55**, 816-827,  
23 doi:10.1109/TGRS.2016.2615552.

1

2 Kummerow, C., W. Barnes, T. Kozu, J. Shiue, and J. Simpson, 1998: The Tropical Rainfall

3 Measuring Mission (TRMM) sensor package, *J. Atmos. Oceanic Technol.*, **15**, 809-817,

4 doi:10.1175/1520-0426(1998)015<0809:TTRMMT>2.0.CO;2.

5

6 Kunkee, D. B., G. A. Poe, D. J. Boucher, S. D. Swadley, Y. Hong, J. E. Wessel, and E. A.

7 Uliana, 2008: Design and evaluation of the first special sensor microwave imager/sounder, *IEEE*

8 *Trans. Geosci. Remote Sens.*, **46**, 863-883, doi:10.1109/TGRS.2008.917980.

9

10 McKague, D. S., C. S. Ruf, and J. J. Puckett, 2011: Beam spoiling correction for spaceborne

11 microwave radiometers using the two-point vicarious calibration method, *IEEE Trans. Geosci.*

12 *Remote Sens.*, **49**, 21-27, doi:10.1109/TGRS.2010.2068052.

13

14 Moradi, I., H. Meng, R. R. Ferraro, and S. Bilanow, 2013: Correcting geolocation errors for

15 microwave instruments aboard NOAA satellites, *IEEE Trans. Geosci. Remote Sens.*, **51**, 3625-

16 3637, doi:10.1109/TGRS.2012.2225840.

17

18 Poe, G. A., E. A. Uliana, B. A. Gardiner, T. E. vonRenzell, and D. B. Kunkee, 2008:

19 Geolocation error analysis of the Special Sensor Microwave Imager/Sounder, *IEEE Trans.*

20 *Geosci. Remote Sens.*, **46**, 913-922, doi:10.1109/TGRS.2008.917981.

21

22 Ruf, C., 2018: *Personal Communication*.

23

Shiue, J., 1997: TMI alignment and other coefficients for the TMI database at TRMM, NASA Internal Memorandum, 6 pp.

Stocker, E. F., F. Alquaied, S. Bilanow, Y. Ji, and L. Jones, 2018: TRMM version 8 reprocessing improvements and incorporation into the GPM data suite, *J. Atmos. Oceanic Technol.*, doi:10.1175/JTECH-D-17-0166.1, *in press*.

Wentz, F. J., P. Ashcroft, and C. Gentemann, 2001: Post-launch calibration of the TRMM microwave imager, *IEEE Trans. Geosci. Rem. Sens.*, **39**, 415-422, doi:10.1109/36.905249.

Wentz, F. J., 2015: A 17-yr climate record of environmental parameters derived from the Tropical Rainfall Measuring Mission (TRMM) Microwave Imager, *J. Climate*, **28**, 6882-6902, doi:10.1175/JCLI-D-15-0155.1.

Wentz, F. J. and D. Draper, 2016: On-orbit absolute calibration of the Global Precipitation Measurement Microwave Imager, *J. Atmos. Oceanic Technol.*, **33**, 1393-1412, doi:10.1175/JTECH-D-15-0212.1.

Yang, J. X., D. S. McKague, and C. S. Ruf, 2016: Boreal, temperate and tropical forests as vicarious calibration sites for spaceborne microwave radiometry, *IEEE Trans. Geosci. Remote Sens.*, **54**, 1035-1051, doi10.1109/TGRS.2015.2472532.

Table 1: Cone angles and azimuth start angles calculated for TMI V8 data release, comparing the values derived here (V8) with Wentz (2015).

Channel	Cone Angle (V8)	Cone Angle Offset (V8)	Cone Angle (Wentz)	Azimuth Start Angle (V8)	Azimuth Start Angle (Wentz)
10v/h	49.45	0.045	49.43	-63.91	-63.70
19v – 85h	49.28	--	49.30	-64.36	-64.10

Fig. 1: Yaw 0 – Yaw 180 gridded TMI TAs over South America for V7 geolocation. Incorrect alignment results in the appearance of coastlines, which can be seen in all channels but is most pronounced in 10h..... 24

Fig. 2: Coastline mask of Yaw 0 – Yaw 180 gridded TMI TAs used for alignment analysis shown for the 10 GHz channels. The RMS of TA differences contained in the mask is used as a metric for determining optimal alignment values..... 25

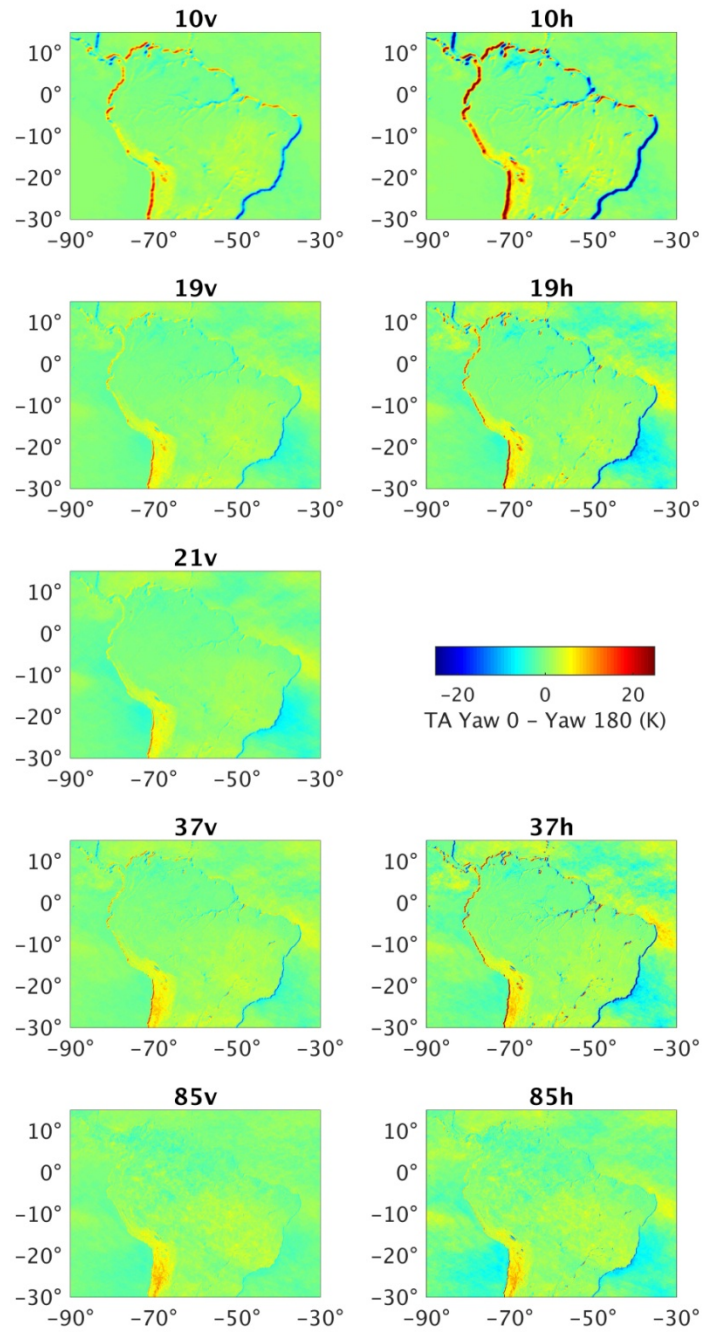
Fig. 3: RMS of the TA difference coastline mask for 19v as a function of cone (top) and azimuth (bottom) angles. A 3<sup>rd</sup> order polynomial is fit to the RMS and the angle where this curve is at a minimum is taken as the optimal cone or azimuth angle for the channel. .... 26

Fig. 4: TMI TA cold and warm along-scan biases calculated using vicarious calibration techniques. The large- and small-scale fluctuations are similar at both TAs, but the edge-of-scan and overall patterns have some significant differences. .... 27

Fig. 5: TA warm minus cold along-scan bias for the whole scan (black line) and the middle of the scan (green line), shown as a difference from the mean. The difference between the v-pol channels (left) and h-pol channels (right) indicates a pitch and/or roll offset. .... 28

1	Fig. 6: Modeled effect of a cone angle (blue line), pitch (yellow line), and roll (green line) offset	
2	on the TMI scan geolocation from nominal (black line), assuming the TRMM spacecraft is	
3	located at (0,0) and the center of the TMI swath is looking forward. The degree of offset is	
4	exaggerated to see effect. This behavior across the scan is used to distinguish a pitch and	
5	roll offset from a cone angle offset. ....	29
6	Fig. 7: Cone angle derivation at left, middle, and right portions of the TMI scan. The consistent	
7	difference between the scans at all channels suggests a pitch and/or roll correction is	
8	needed. ....	30
9	Fig. 8: The variation in the cone angle across the scan is used to derive a pitch/roll angle by	
10	fitting a curve of the off-nadir angle as a function of azimuth angle. The curve for 19v is	
11	shown here as an example.....	30
12	Fig. 9: Derived pitch and roll offsets for all channels. The average offset is $-0.08^\circ$ for both pitch	
13	and roll. ....	31
14	Fig. 10: TMI cone (top) and azimuth (bottom) angles derived from geolocation analysis. The two	
15	feedhorns give significantly different results.....	32
16	Fig. 11: Yaw 0 – Yaw 180 gridded TMI TAs over South America for updated instrument attitude	
17	and cone and azimuth angles to be used in V8. The geolocation for all channels is greatly	
18	improved compared to Fig. 1. ....	33
19	Fig. 12: Comparison of V7 (black), V8 cold (blue), and V8 warm (red) estimates of TMI scan	
20	biases. The V7 method assumes these biases are constant as a function of scene	
21	temperature, so the new biases can differ significantly at the edge of scan (e.g. $\sim 1\text{K}$ right	
22	side of 19h scan). The pitch/roll offset included in V8 results in greater agreement between	
23	cold and warm biases for the middle of the scan. ....	34

1  
2



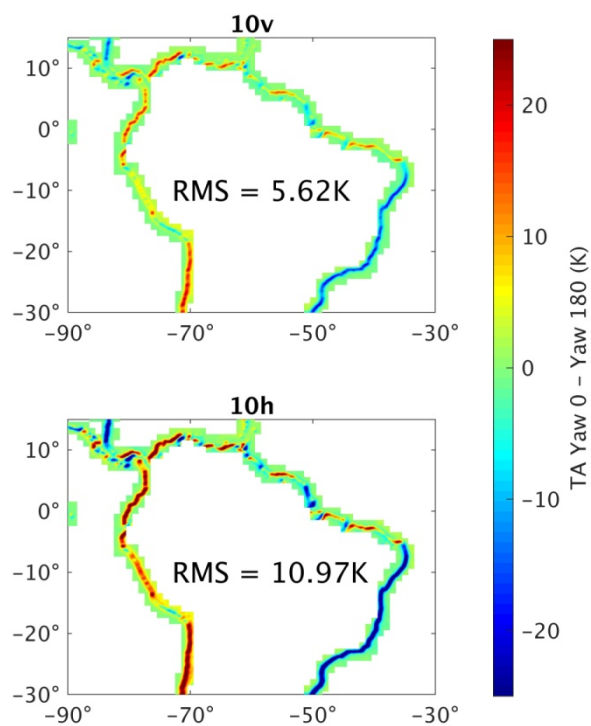
3  
4  
5  
6

Fig. 1: Yaw 0 – Yaw 180 gridded TMI TAs over South America for V7 geolocation. Incorrect alignment results in the appearance of coastlines, which can be seen in all channels but is most pronounced in 10h.



1

2



3

4

Fig. 2: Coastline mask of Yaw 0 – Yaw 180 gridded TMI TAs used for alignment analysis

5

shown for the 10 GHz channels. The RMS of TA differences contained in the mask is used as a

6

metric for determining optimal alignment values.

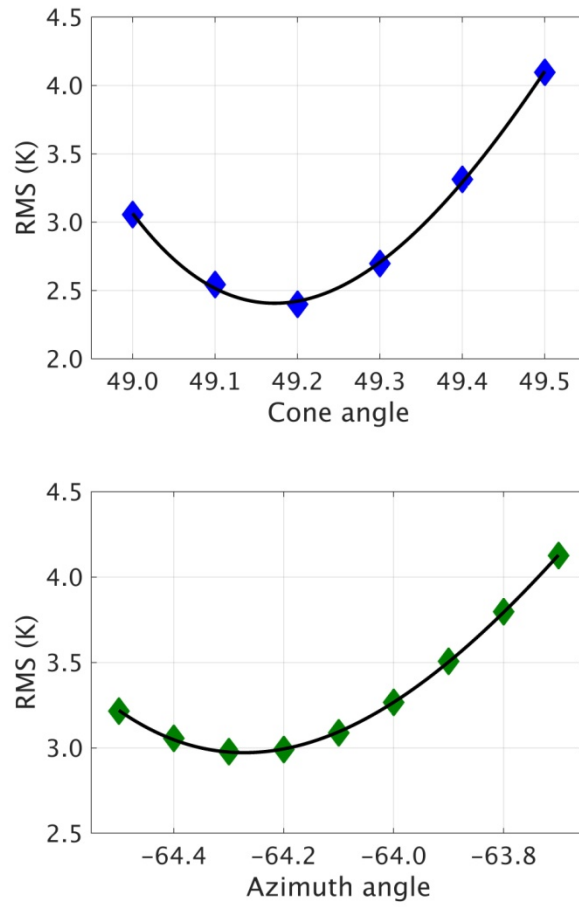


Fig. 3: RMS of the TA difference coastline mask for 19v as a function of cone (top) and azimuth (bottom) angles. A 3<sup>rd</sup> order polynomial is fit to the RMS and the angle where this curve is at a minimum is taken as the optimal cone or azimuth angle for the channel.

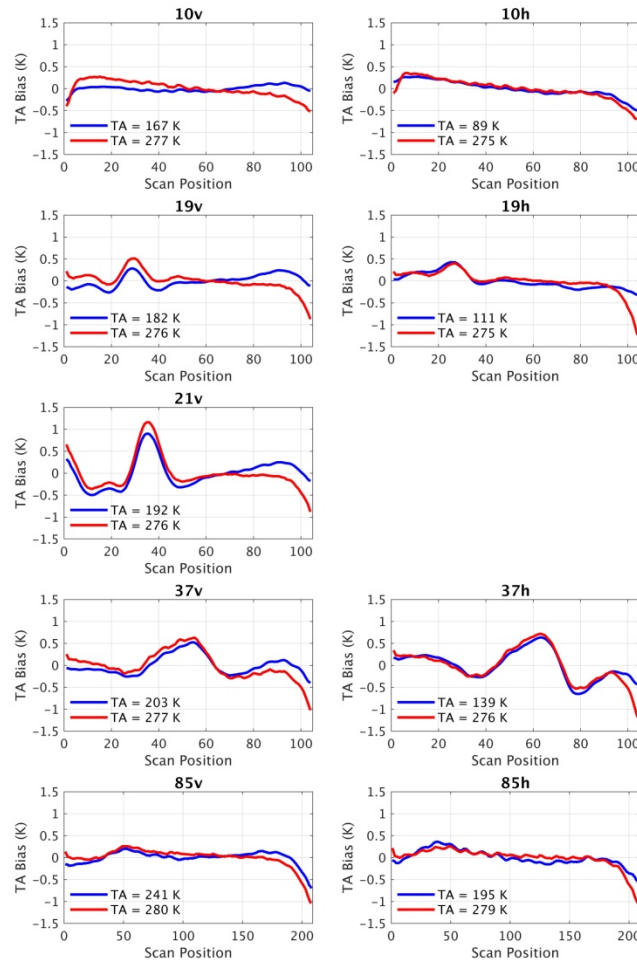
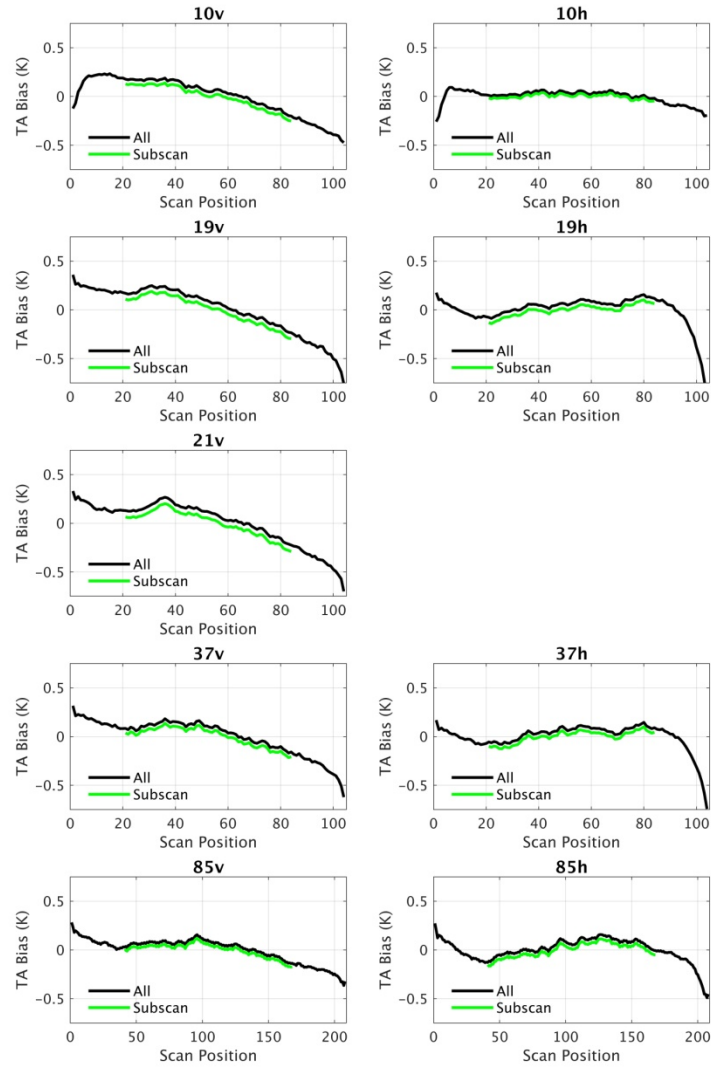


Fig. 4: TMI TA cold and warm along-scan biases calculated using vicarious calibration techniques. The large- and small-scale fluctuations are similar at both TAs, but the edge-of-scan and overall patterns have some significant differences.

1



2

3

4

5

6

Fig. 5: TA warm minus cold along-scan bias for the whole scan (black line) and the middle of the scan (green line), shown as a difference from the mean. The difference between the v-pol channels (left) and h-pol channels (right) indicates a pitch and/or roll offset.

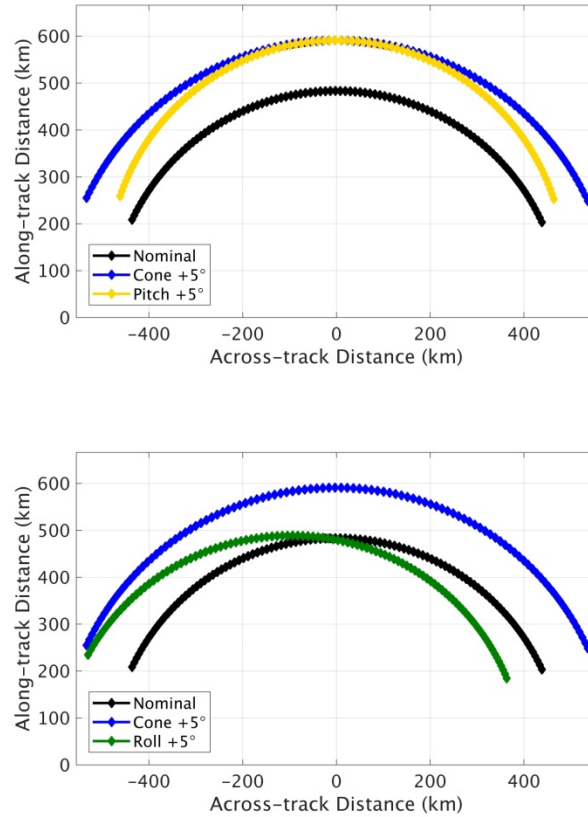


Fig. 6: Modeled effect of a cone angle (blue line), pitch (yellow line), and roll (green line) offset on the TMI scan geolocation from nominal (black line), assuming the TRMM spacecraft is located at (0,0) and the center of the TMI swath is looking forward. The degree of offset is exaggerated to see effect. This behavior across the scan is used to distinguish a pitch and roll offset from a cone angle offset.

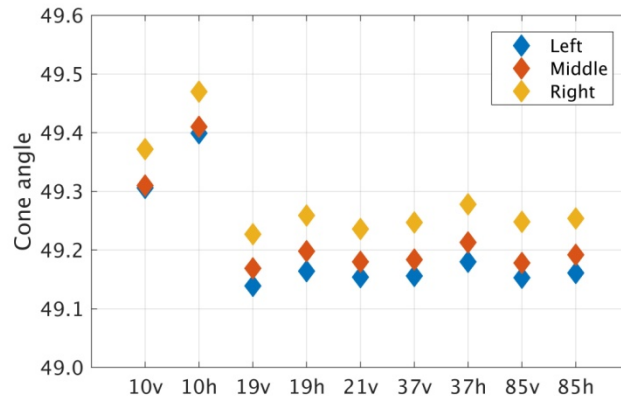


Fig. 7: Cone angle derivation at left, middle, and right portions of the TMI scan. The consistent difference between the scans at all channels suggests a pitch and/or roll correction is needed.

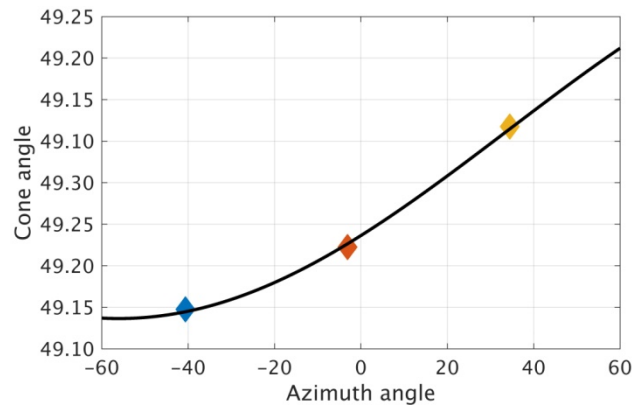
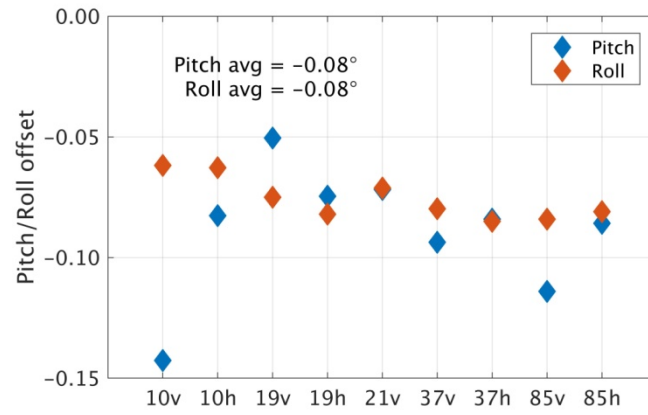


Fig. 8: The variation in the cone angle across the scan is used to derive a pitch/roll angle by fitting a curve of the off-nadir angle as a function of azimuth angle. The curve for 19v is shown here as an example.

1

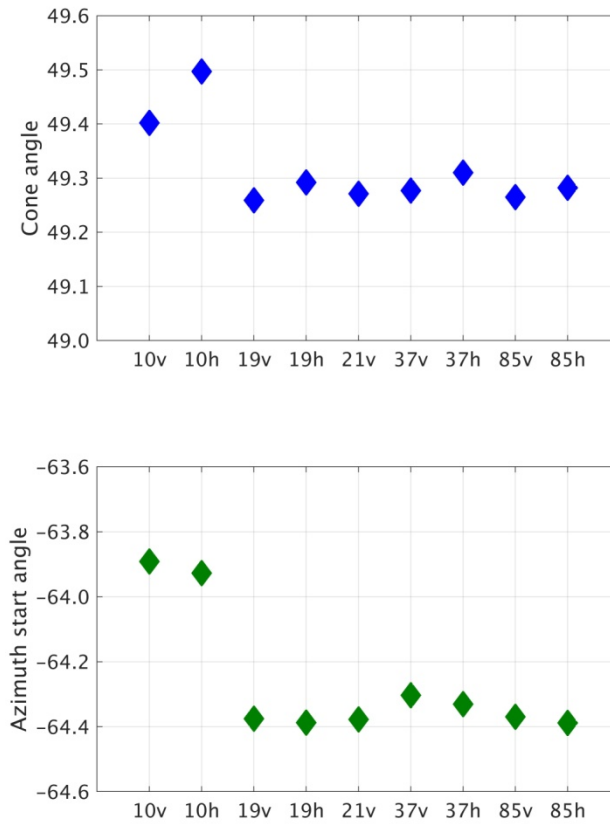


2

3 Fig. 9: Derived pitch and roll offsets for all channels. The average offset is  $-0.08^\circ$  for both pitch  
4 and roll.

5

1  
2

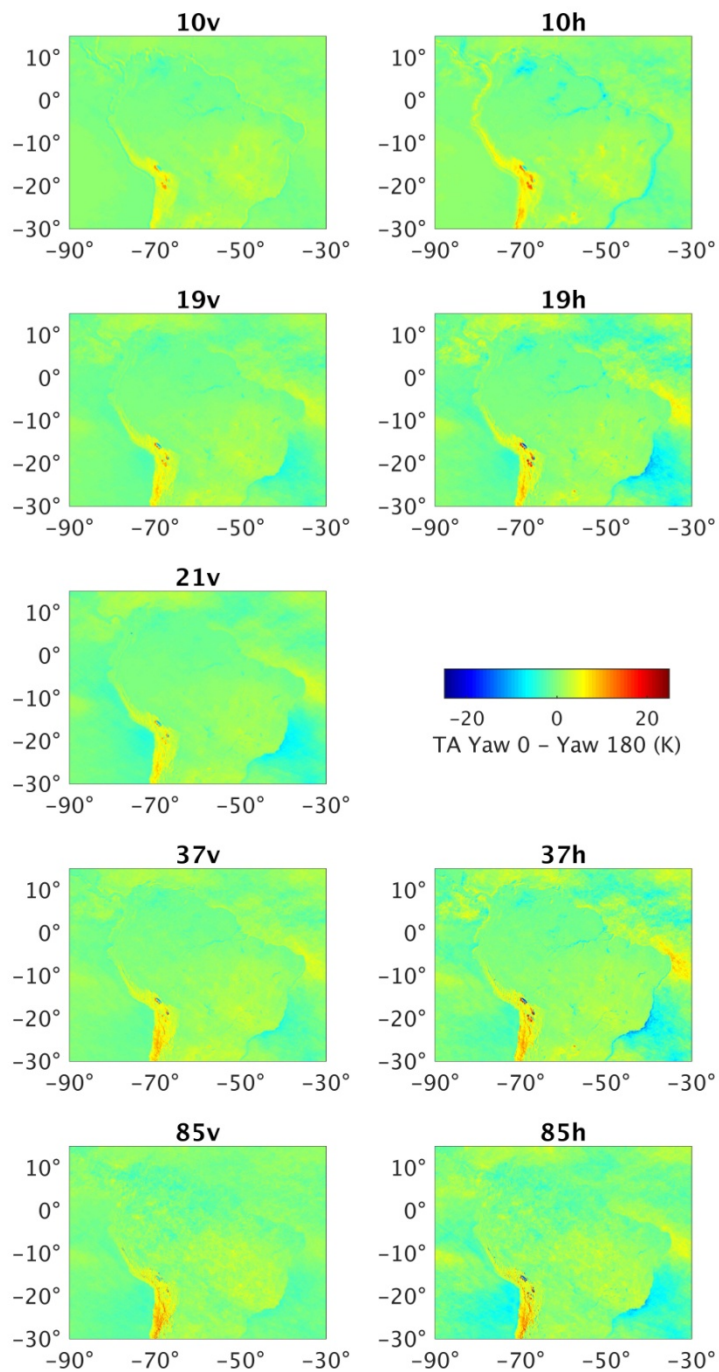


3  
4  
5  
6

Fig. 10: TMI cone (top) and azimuth (bottom) angles derived from geolocation analysis. The two feedhorns give significantly different results.



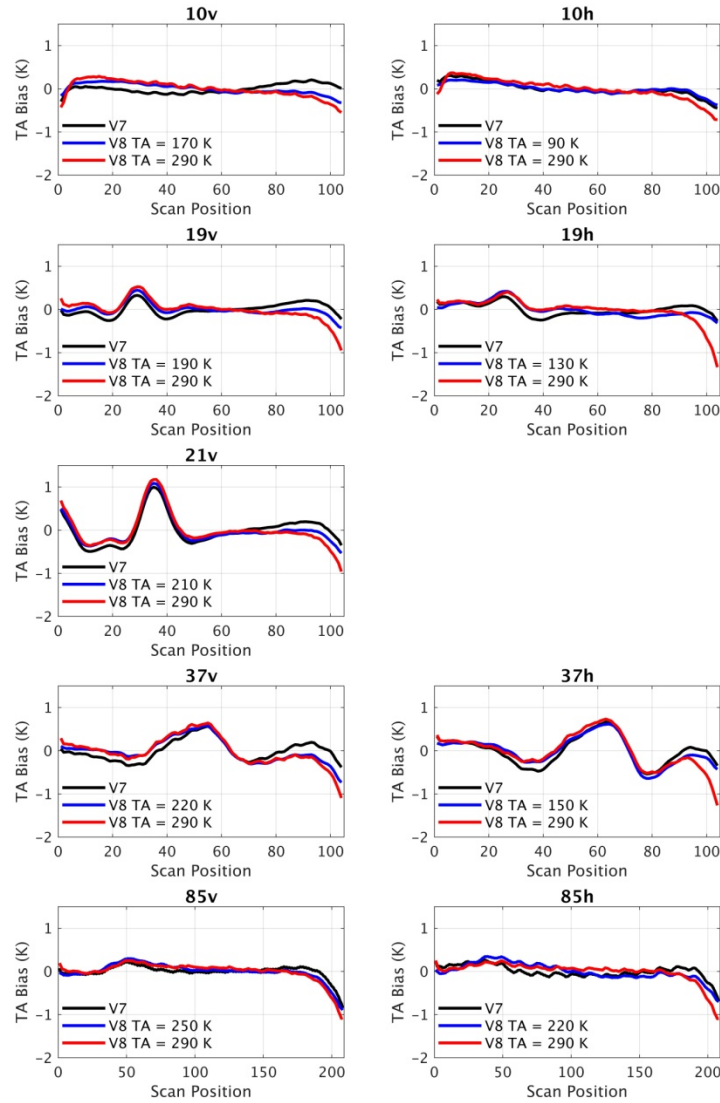
1



2

3 Fig. 11: Yaw 0 – Yaw 180 gridded TMI TAs over South America for updated instrument attitude  
 4 and cone and azimuth angles to be used in V8. The geolocation for all channels is greatly  
 5 improved compared to Fig. 1.

1  
2



3

4

5

6

7

8

Fig. 12: Comparison of V7 (black), V8 cold (blue), and V8 warm (red) estimates of TMI scan biases. The V7 method assumes these biases are constant as a function of scene temperature, so the new biases can differ significantly at the edge of scan (e.g.  $\sim 1\text{K}$  right side of 19h scan). The pitch/roll offset included in V8 results in greater agreement between cold and warm biases for the middle of the scan.